JOURNAL OF SPACECRAFT AND ROCKETS
Vol. 45, No. 5, September–October 2008

Detached Eddy Simulations and Reynolds-Averaged Navier–Stokes Calculations of a Spinning Projectile

Sriram Doraiswamy* and Graham V. Candler†
University of Minnesota, Minneapolis, Minnesota 55455

DOI: 10.2514/1.31935

Reynolds-averaged Navier–Stokes and detached eddy simulations are performed on a 0.50 caliber spinning projectile for three yaw angles over the Mach number range of 0.6–2.7. The simulations are compared with the experimental data of McCoy (McCoy, R. L., "The Aerodynamic Characteristics of 0.50 Ball, M33, API, M8, and APIT, M20 Ammunition," U.S. Army Ballistic Research Lab. BRL-MR-3810, Aberdeen Proving Ground, MD, Jan. 1990) and the Reynolds-averaged Navier–Stokes results of Silton (Silton, S., "Navier-Stokes Computations for a Spinning Projectile from Subsonic to Supersonic Speeds," *Journal of Spacecraft and Rockets*, Vol. 42, No. 2, 2005, pp. 223–231). Unlike the Reynolds-averaged Navier–Stokes simulations, the detached eddy simulations are shown to predict unsteady base and wake flows, which affect the predicted aerodynamic behavior of the projectile. There are some notable differences between the predictions of the present Reynolds-averaged Navier–Stokes simulations and those of Silton; they are most likely a result of the different turbulence models used. This further illustrates the sensitivity of the results to the turbulence modeling approach, for both Reynolds-averaged Navier–Stokes and detached eddy simulations. The largest difference between Reynolds-averaged Navier–Stokes and detached eddy simulations is found for the Magnus moment coefficient at small yaw angles. Analysis shows that this moment is particularly sensitive to the unsteady wake and shock motion predicted by detached eddy simulations.

Nomenclature

C_D	=	drag coefficient, $D/\frac{1}{2}\rho V_\infty^2 S$
C_{D0}	=	zero yaw drag coefficient
$C_{L\alpha}$	=	lift-force coefficient derivative, $L/\frac{1}{2}\rho V_\infty^2 S\delta$
C_{lp}	=	roll-damping coefficient, roll-damping moment/ $\frac{1}{2}\rho V_\infty^2 S(p_s d/V_\infty)$
C_{Mp}	=	Magnus moment coefficient, Magnus moment/ $\frac{1}{2}\rho V_\infty^2 Sd(p_s d/V_\infty)$
$C_{Mp\alpha}$	=	Magnus moment coefficient derivative, Magnus moment/ $\frac{1}{2}\rho V_\infty^2 Sd(p_s d/V_\infty)\delta$
$C_{M\alpha}$	=	overturning moment coefficient derivative, static moment/ $\frac{1}{2}\rho V_\infty^2 Sd(p_s d/V_\infty)\delta$
$C_{Np\alpha}$	=	Magnus force coefficient derivative, Magnus force/ $\frac{1}{2}\rho V_\infty^2 S(p_s d/V_\infty)\delta$
C_p	=	pressure coefficient, $(p - p_\infty)/\frac{1}{2}\rho V_\infty^2$
D	=	drag force, N
d	=	reference diameter, m
L	=	lift force, N
M	=	Mach number
p	=	pressure, N/m^2
p_s	=	roll rate, rad/s
S	=	reference area, $\pi d^2/4$
V_∞	=	freestream velocity, m/s
y^+	=	normal viscous sublayer spacing
α	=	angle of yaw, deg
α_t	=	total angle of yaw, $\sqrt{\alpha^2 + \beta^2}$
β	=	sideslip angle, deg
δ	=	$\sin\alpha$
ρ	=	air density, kg/m^3
τ_f	=	flow time, d/V_∞

Received 3 May 2007; revision received 5 February 2008; accepted for publication 7 April 2008.

*Graduate Research Assistant.
†Professor.

I. Introduction

THE estimation of forces and moments acting on a spinning projectile is crucial to the accurate prediction of its trajectory. The forces and moments on the projectile also determine the stability characteristics of the projectile. In particular, the Magnus force and moment, although small in magnitude, play an important role in the dynamic stability of the projectile. Hence, it is critical that these be predicted accurately for improved design of projectiles. The Magnus force is the force that arises because of the distorted boundary layer due to spin. The focus of interest has been on understanding this phenomenon and its relation to the spin rate and angle of yaw. Many experimental and computational studies have investigated these forces and moments, starting from simple geometries, such as cones and slender bodies, to projectiles with complicated configurations, such as those with boat tail shapes and fins.

A number of computational techniques have been used to estimate the different aerodynamic coefficients. Early numerical studies used simplified flow models to study the Magnus force and moment [1–5]. To study the flow over an arbitrary projectile body, techniques such as the parabolized Navier–Stokes (PNS) method were adopted. The PNS approach was extensively used for studying supersonic flow over spinning projectiles. The projectile shapes investigated included the cone, the ogive cylinder, and the ogive cylinder boat tail [6]. Excellent agreement was observed for lower angles of yaw at supersonic Mach numbers. This computational approach was also used to calculate other coefficients, such as the pitch damping coefficients, although it was limited to supersonic and hypersonic flows [7]. Guidos and Chung performed supersonic computations using the PNS method on a 0.50 cal. projectile similar to the projectile investigated in the present study and obtained good agreement with experiments [8]. The PNS method was also used to study the behavior of the Magnus forces at lower supersonic velocities [9]. The results showed a fair comparison and qualitative agreement with experiments.

With the advancement of computer technology, full three-dimensional computations were used to estimate the forces and moments on spinning projectiles with different configurations [10–13]. Steady-state simulations on spinning projectiles have been carried out to determine the aerodynamic coefficients with reasonable accuracy. Recently, detached eddy simulations (DES) have been widely used to carry out unsteady simulations. DES is a hybrid Reynolds-averaged Navier–Stokes (RANS)/large eddy

simulations (LES) approach based on the Spalart–Allmaras turbulence model [14] that allows for the large-scale turbulent structures of the flow to be captured, whereas the near wall region is simulated with RANS, reducing the resolution required at the wall. Because the flow is separated near the base, and DES has been shown to perform well for separated flows [15,16], it is not unreasonable to assume that DES might improve the quality of the results for the various aerodynamic coefficients. In a recent study by DeSpirito and Heavey, aerodynamic coefficients were estimated using different steady-state turbulence models and a hybrid RANS/LES model based on the cubic k–ϵ model [17]. The hybrid RANS/LES model was found to produce better results than steady-state turbulence models, especially for the Magnus moment coefficient. The ability of the hybrid model to predict the oscillatory nature of the wake was attributed to the improvement observed in the results. The effect of yaw on different aerodynamic coefficients using the hybrid model was not investigated.

To the best of our knowledge, time-accurate unsteady simulations have not been carried out for an entire Mach number range for different yaw angles. The motivation of the current study is to make comparisons between the widely used RANS modeling approach and the more recently developed DES approach. In particular, we are interested in how the unsteady flow physics captured by DES affects the projectile aerodynamics. We also compare our results to the RANS results of Silton [18] to assess the sensitivity of the predictions to the turbulence model. In the present work, both steady and unsteady simulations are performed on the 0.50 cal. projectile investigated in [18,19]. A three-dimensional unstructured finite volume solver (US3D) [20] developed at the University of Minnesota is used in the present study. The simulations were run for a total of 12 Mach numbers from subsonic to supersonic velocities at three different yaw angles (as in [18]). The results obtained are compared with the experiments [19] and with the steady-state results obtained by Silton [18].

II. Numerical Approach

A. Model Geometry and Grid

The model used for the present study, as mentioned earlier, is the 0.50 cal. (1 cal. = 12.95 mm) axisymmetric projectile (Fig. 1) investigated in [18,19]. The projectile has a 0.16-cal.-long, 0.02-cal.-deep groove, and a 9 deg filleted boattail. The total length of the model is 4.46 cal. The center of gravity is located at 2.68 cal. from the nose.

The grids used in all the simulations were generated using GridPro [21]. The grid design in Silton [18] was used to guide grid generation. The grids are composed of unstructured hexahedral meshes. For the purpose of steady-state RANS simulations, two fine-resolution grids were generated; one was for the subsonic and transonic conditions, and the other was for the supersonic cases. The grid is axisymmetric with 120 points in the circumferential direction. The groove has 30 points along the axis, and there are 50 points in the radial direction within the groove. The structure of the grid close to the projectile is the same for both the supersonic and subsonic grids. The medium and coarse grids were generated with the purpose of grid resolution study by successively coarsening the fine-resolution grid in all directions. The medium and coarse grids have 104 points and 88 points in the circumferential direction, respectively. Cells were removed from the base and the groove to obtain the medium and coarse grids. To resolve the boundary layer reasonably, the first radial surface spacing was set at 0.5 μm so as to obtain a $y^+ < 1$ for all simulations. The three grids, grid 1 (2.7 million cells), grid 2 (3.2 million cells), and grid 3 (5.3 million cells), were used for the grid resolution study.

DES require the use of more grid points both at the groove and in the base region to adequately capture unsteady vortical structures in the flowfield and fewer grid points in the far field. Similar to the steady-state simulations, three grids were generated, one each for the subsonic and supersonic cases and a third grid for the supersonic case for the purpose of a grid resolution study. Because DES is known to perform very well in separated regions [22], the structure of the grids was altered to focus on the regions of separation, such as the base and the groove. A large number of grid points was used near the base to adequately refine the flow separation region. The groove did not have any characteristic flow features that demanded the same amount of resolution as the base. Similar to the grids generated in the RANS case for the purpose of grid resolution study, a medium grid and a coarse grid were obtained for the DES case by coarsening the fine-resolution grid in all directions. As in the RANS case, the medium and coarse grids have 104 points and 88 points along the circumferential direction; also, the base, the groove, and the wake region were coarsened to obtain the medium and coarse grids. The first radial wall spacing was fixed for all the three grids. The three grids, grid 4 (3.0 million cells), grid 5 (3.6 million cells), and grid 6 (6.0 million cells), were used for the grid resolution study. Because the Magnus force is generated by spin-induced distortion of the boundary layer, it is important that the boundary layer be well captured. Hence, the first radial spacing was fixed at 0.25 μm to obtain a $y^+ < 0.5$ [17]. Figures 2 and 3 compare computational grids used for RANS and DES for the subsonic and supersonic cases. Figure 4 shows the contrast in the forebody, groove, and base regions between the RANS and DES grids.

The outer boundaries of all the grids were created such that no interference with the flowfield occurred at any of the flow regimes. The inflow boundary was three body lengths away for the subsonic grid and under a body length for the supersonic grid. The outflow boundary was situated 10 body lengths away for the subsonic grid and five body lengths away for the supersonic grid. The circumferential boundary was six body lengths away from the surface for the subsonic grid and three body lengths away for the supersonic case. An isothermal wall ($T = 288$ K) boundary condition was used at the projectile body. The velocity at the wall was set in accordance with the angular velocity. The freestream conditions used were $\rho_\infty = 1.225$ kg/m^3 and $T_\infty = 288$ K. The velocity of the freestream was varied from a Mach number of 0.6 to 2.7.

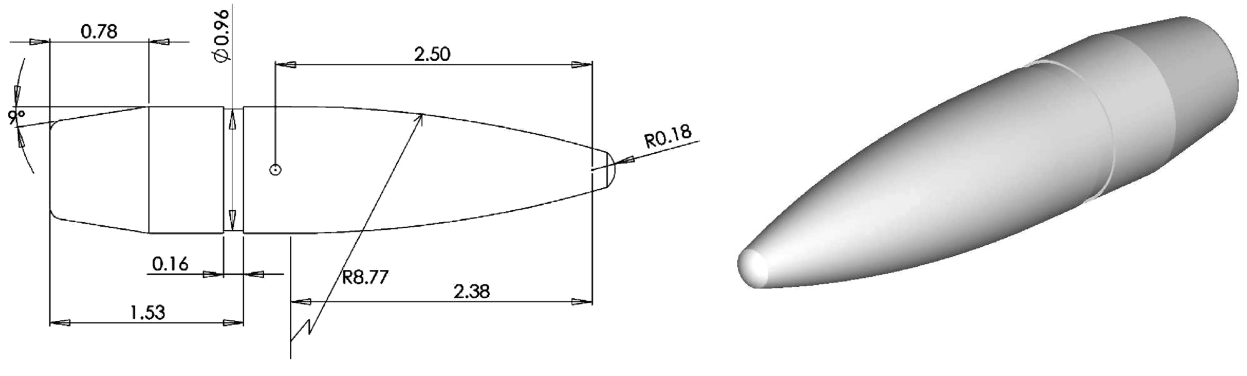

Fig. 1 The 0.05 cal. projectile: a) sketch with all dimensions in calibers[18], and b) the computational model.

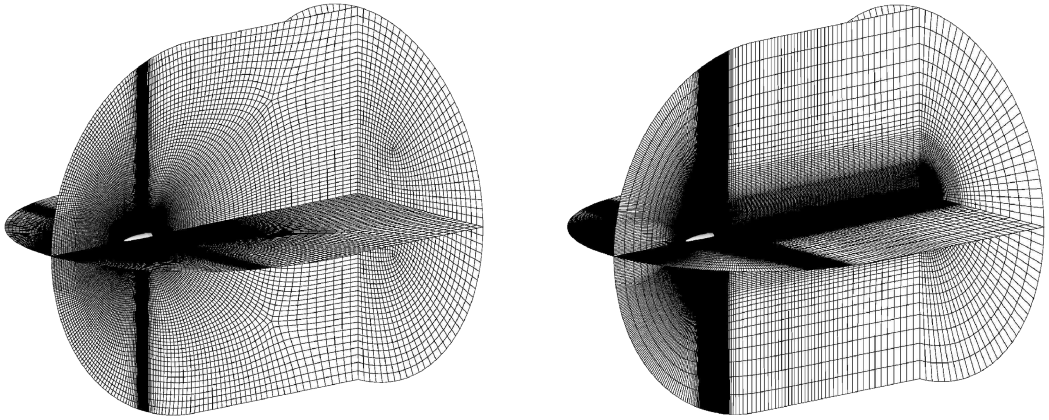

a) b)

Fig. 2 Computational grid used for subsonic cases $M < 1.5$: a) RANS, and b) DES.

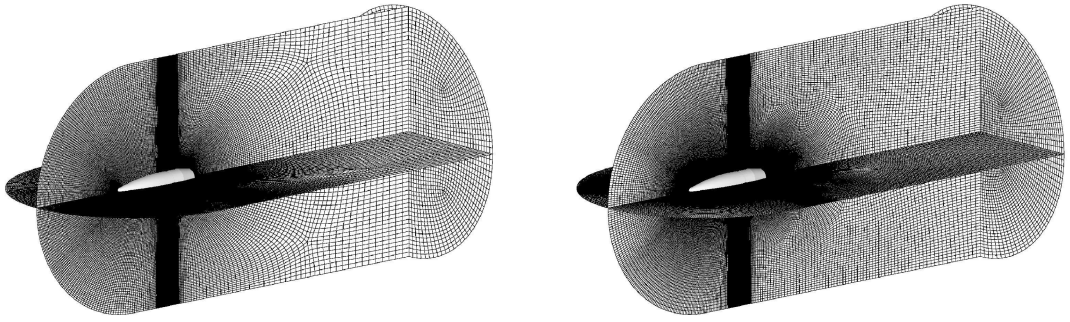

a) b)

Fig. 3 Computational grid used for supersonic cases $M > 1.5$: a) RANS and b) DES.

B. Flow Solver

A hybrid, implicit unstructured finite volume solver that solves the compressible Navier–Stokes equations is used to compute the flowfield [20]. The inviscid fluxes are calculated using a low dissipation version of Steger–Warming flux vector splitting [23]. This uses exact linearization of the fluxes and upwind biasing using the signs of the eigenvalues. Second- or third-order accuracy is achieved by using an upwind biased monotone upstream-centered scheme for conservation laws approach. The viscous fluxes are evaluated using weighted least-squares fits with the deferred correction approach suggested by Kim et al. [24], and the turbulence source terms are evaluated using second-order accurate central differencing. Turbulence closure is obtained by the use of the Spalart–Allmaras one-equation model [14] with density corrections by Catris and Aupoix [25]. The solver may be run in both RANS and DES modes. Time integration is performed implicitly. A parallel line relaxation procedure [26] is used in areas where the grids are severely stretched and the lines of the grids can be assembled (near the surfaces). In regions where such construction cannot be achieved, a full-matrix point relaxation [27] method is adopted. This approach is described in detail in [20,28]. The full-matrix point relaxation method is used for the time-accurate simulations so as not to bias the solution [29].

III. Results and Discussion

Simulations were carried out for a wide range of Mach numbers from the subsonic to the supersonic regime. The conditions for the simulations are the same as in [18]. A total of 12 Mach numbers were studied for three different angles of yaw, −0, 2, and 5 deg. Table 1 lists the different Mach numbers along with the respective frequencies for the spin of the projectile. More cases in the transonic regime were investigated to capture both the fast changing characteristics of the flowfield and to study the variation in force and moment coefficients. All simulations were performed in parallel using dual-core 2.2 GHz Opteron processors. The simulations of the steady cases were run on 48 cores. The simulations were considered to be converged when the residuals dropped by 3–4 orders of magnitude. Additionally, it was also required that the aerodynamic coefficients vary less than 1% on average [18]. This typically took about 2–4 h depending on the Mach number for the steady-state simulations. In the supersonic cases, about 2000 time steps were performed to obtain convergence; transonic and subsonic simulations converged in about 3000 time steps.

Simulations of the unsteady cases used 60 cores because time-dependent statistics were required. Time-dependent statistics were extracted after the residual stabilized, and this usually occurred after about 2000 time steps. The time step used for the simulations ranged from 0.3 μs for the $M = 2.7$ case to 0.9 μs for the $M = 0.6$ case. The time step was chosen to keep the Courant–Friedrichs–Lewy (CFL) number in the separated base flow region at less than 1 to assure time accuracy and resolve all major frequencies [29]. The unsteady simulations were run for a longer period for subsonic and transonic cases than the supersonic cases. Simulations were run for about 100 flow times (1 flow time is defined as $\tau_f = d/V_\infty$) for the supersonic cases, and about 250 flow times for subsonic and transonic cases. These simulations took about 16 h for the supersonic cases and about 24–48 h for the subsonic and transonic cases. For both the steady-state and time-accurate simulations, several cases were run at $M = 1.5$ on both the transonic and the supersonic grid to check for consistency. Results obtained from the two grids matched within 1%.

A. Grid Resolution Study

A grid resolution study was carried out for the steady and unsteady simulations. Following [18], the $M = 2.7$ case was selected for grid resolution study at $\alpha = 0$, 2, and 5 deg. This Mach number has the

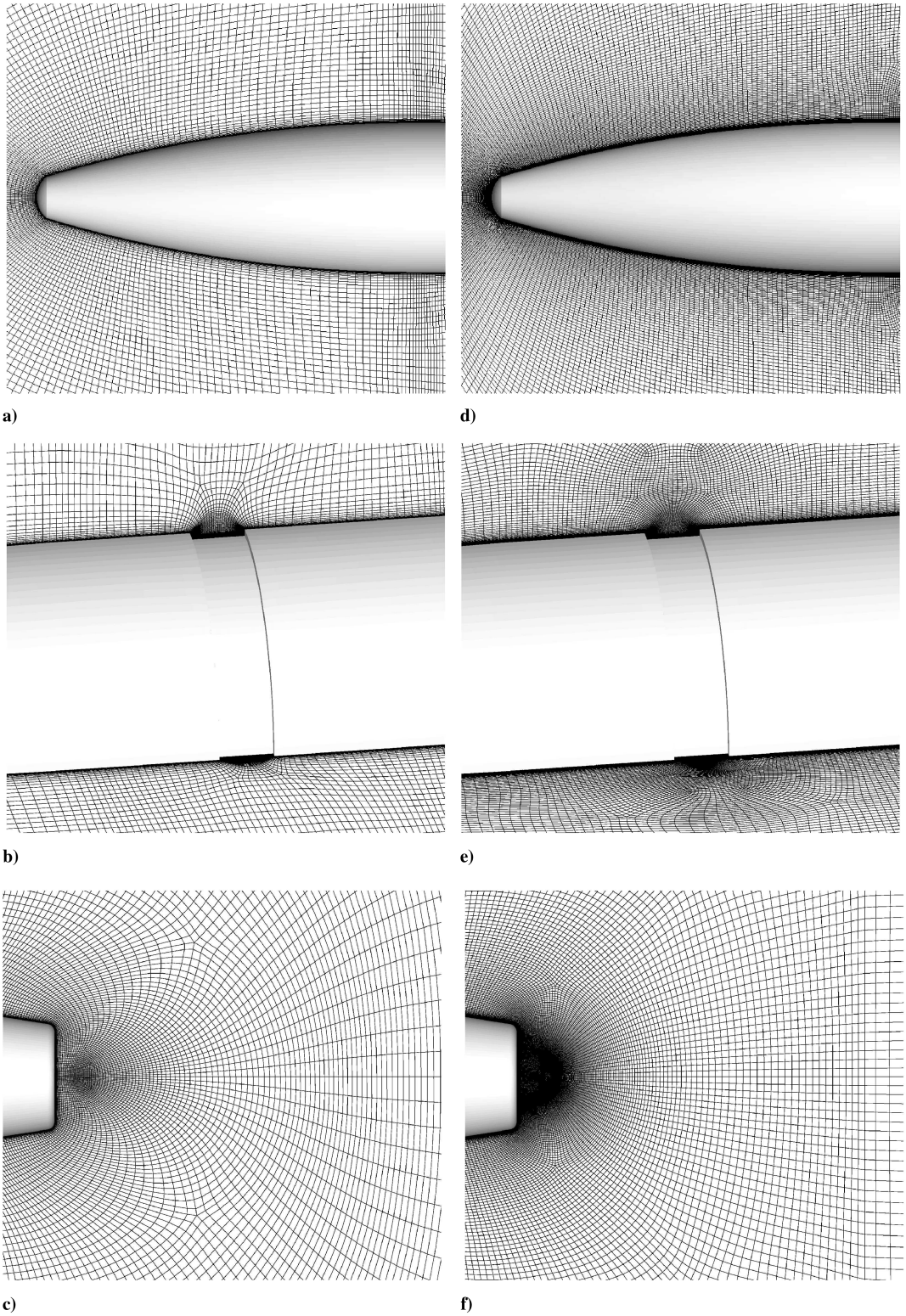

Fig. 4 A closer look at the computational grid used for RANS: a) forebody, b) groove, c) base and DES, d) forebody, e) groove, and f) base.

thinnest boundary layer and most distinct flow physics [18]. The results were compared with the nearest data point from the M33 and M8 experiments obtained by McCoy [19]. Tables 2 and 3 provide a comparison between the present RANS results with the experiments and steady-state results from [18] for the three grids. In Table 2, results for $\alpha = 0$ deg are listed for the drag and roll-damping coefficients. The change in the drag coefficient is about 2% and the change in the roll-damping coefficient is close to 10% between grids 2 and 3. Both the coefficients are within 5% of the experimental value for grid 3. The values also agree very well with the results in [18]. Table 3 lists the results for the 2 and 5 deg angle of yaw cases. The differences in steady-state coefficients such as lift force and overturning moments are less than 1% between the grids for both the 2 and 5 deg angles of yaw cases. The difference in the roll-damping coefficient between grids 2 and 3 for both the angles of yaw was about 10%. The roll-damping moment is found to be very sensitive to the number of cells in the circumferential direction. The maximum difference in drag was found to be of the same order for the 2 and 5 deg cases (about 3%). The difference in Magnus forces and moments were larger. The maximum variation between the three

Table 1 Flowfield conditions and spin rates used in the simulations

Mach number	Spin rate, rad/s
0.60	3366.9
0.70	3927.9
0.85	4768.5
0.90	5050.3
0.94	5274.7
0.98	5499.2
1.05	5892.0
1.10	6172.5
1.25	7014.2
1.50	8417.0
2.00	11,222.8
2.70	15,150.6

Table 2 Grid resolution study for $M = 2.7$ for $\alpha = 0$ deg for RANS

Case	C_D	C_{lp}
Grid 1	0.3047	−0.01019
Grid 2	0.3023	−0.00812
Grid 3	0.2953	−0.00730
[18]	0.2964	−0.00768
M33 experiment [19]	0.279	−0.011

grids was about 4% for the 2 deg case and about 8% for the 5 deg case. Similar results for grid resolution studies were found in [17,18]. The maximum deviation for all the coefficients in [18] was less than 1% for the $\alpha = 0$ deg case and, for $\alpha = 2$ deg, it was less than 0.5% for all the coefficients except C_D and C_{Np_α}. The increase was slightly higher (∼1%) for the other two coefficients. The change in the roll-damping coefficient in [18] was not as high as in this present study because the grids used for the grid resolution study had the same number of cells in the circumferential direction. DeSpirito and Heavey [17] showed a maximum difference of about 1% for the steady-state coefficients such as drag, lift, and pitching moment, and about 3% for the Magnus force coefficient derivative and 11% for the Magnus moment coefficient. Either of the two grids, grids 2 or 3, would have sufficed for the steady-state computations. Because results from fine-resolution grid matched better with the experiments, it was used to run the steady-state simulations.

For the detached eddy simulations, a grid resolution study was carried out for $\alpha = 2$ and 5 deg. Table 4 compares the values of coefficients between the grids at the two yaw angles for $M = 2.7$. The maximum deviation in all the steady-state coefficients was less than 3% for both the 2 and 5 deg cases. The difference in the roll-damping coefficient was less than 10% for both the angles of yaw between grids 5 and 6. The Magnus force and moment derivatives deviated further (∼11%). Determination of the Magnus quantities is quite difficult because the actual magnitude of Magnus force and moment is extremely small compared with the other forces. The difference in the various aerodynamic coefficients was comparable to that of the steady case; they were within 0.5% of the experiments for the finest grid (grid 6). Also, because grid refinement provides a means of increasing the range of length scales in DES [30], the fine-resolution grid was chosen to do the unsteady simulations.

B. Flow Characteristics

Figures 5–9 show the flowfield for different flow regimes for representative Mach numbers. The flowfield comparison between RANS and DES uses the same contour map. The flowfield parameters such as the C_p values and the Mach numbers from current RANS show very good agreement with those obtained by Silton [18] and data presented by Guidos and Chung [8] for similar cases. Figures 5 and 6 compare the Mach number contours for $M = 0.60$ between the RANS and DES solutions for 0 and 2 deg angles of yaw. We see a subsonic flowfield throughout the domain. There is almost no defined flow feature in the base for the RANS case. For $\alpha = 0$ deg, RANS fails to predict any form of unsteadiness in the wake and the flow is axisymmetric. On the contrary, the DES solution exhibits unsteadiness in the wake and shows the presence of

Table 3 Grid resolution study for $M = 2.7$ for $\alpha = 2$ and 5 deg for RANS

		$\alpha = 2$ deg				
Case	C_D	C_{L_α}	C_{Mp_α}	C_{M_α}	C_{Np_α}	C_{lp}
Grid 1	0.3087	2.5592	0.2048	2.8139	0.3646	−0.01019
Grid 2	0.3063	2.5497	0.2131	2.8321	0.3502	−0.00813
Grid 3	0.3000	2.5301	0.2122	2.8268	0.3362	−0.00729
[18]	0.3062	2.23	0.21	2.80	——	−0.00765
M33 experiment [19]	0.2813	2.21	0.15	3.01	——	−0.011
M8 experiment [19]	0.2991	2.42	0.24	2.85	——	−0.011
		$\alpha = 5$ deg				
Case	C_D	C_{L_α}	C_{Mp_α}	C_{M_α}	C_{Np_α}	C_{lp}
Grid 1	0.3228	2.7002	0.2147	2.7694	0.3767	−0.01019
Grid 2	0.3212	2.6997	0.2384	2.7743	0.3623	−0.00813
Grid 3	0.3162	2.6750	0.2350	2.7842	0.3582	−0.00733

Table 4 Grid resolution study for $M = 2.7$ for $\alpha = 2$ and 5 deg for DES

		$\alpha = 2$ deg				
Case	C_D	C_{L_α}	C_{Mp_α}	C_{M_α}	C_{Np_α}	C_{lp}
Grid 4	0.3001	2.5496	0.2042	2.8198	0.2897	−0.010041
Grid 5	0.2973	2.5367	0.2264	2.8217	0.3369	−0.007834
Grid 6	0.2920	2.5264	0.2306	2.8368	0.3564	−0.006993
M33 experiment [19]	0.2813	2.21	0.15	3.01	——	−0.011
M8 experiment [19]	0.2991	2.42	0.24	2.85	——	−0.011
		$\alpha = 5$ deg				
Case	C_D	C_{L_α}	C_{Mp_α}	C_{M_α}	C_{Np_α}	C_{lp}
Grid 4	0.3170	2.6987	0.2347	2.9753	0.3483	−0.01004
Grid 5	0.3156	2.6801	0.2497	2.8823	0.3589	−0.00783
Grid 6	0.3139	2.6778	0.2575	2.7855	0.3819	−0.00700

asymmetry, a characteristic feature of spinning projectiles, even at $\alpha = 0$ deg. The transonic flowfields also have the same characteristics as the subsonic flows, exhibiting unsteadiness in the base region. A marked change in the wake flow is observed between the steady and unsteady simulations. Note the difference in the shock profiles in Fig. 7. The shock at the start of the base in the RANS case is spread much farther than the corresponding DES case. It was also found that the shocks in the transonic flowfield showed signs of

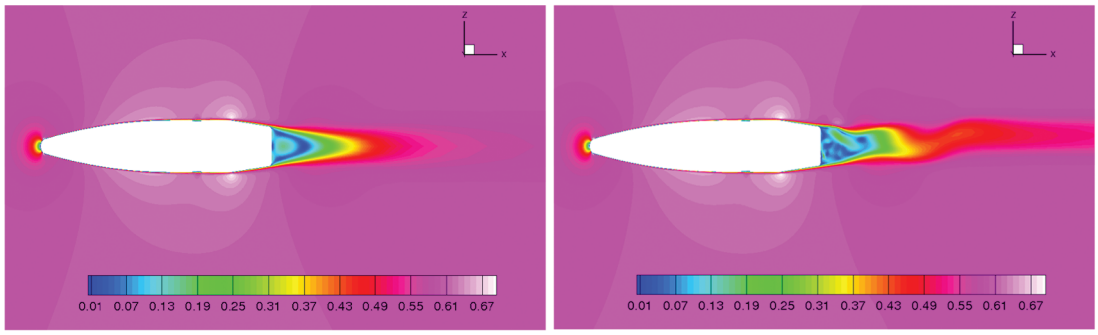

a) b)

Fig. 5 Comparison of Mach number contours at $\alpha = 0$ deg for $M = 0.60$: a) RANS, and b) DES (instantaneous).

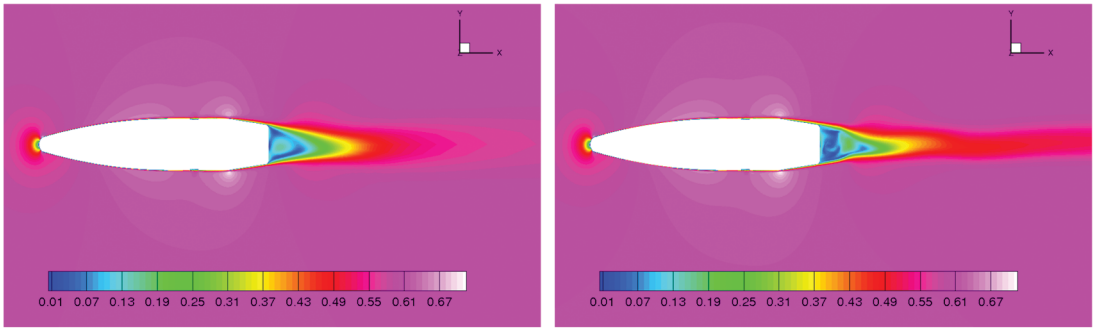

a) b)

Fig. 6 Comparison of Mach number contours on the pitch plane at $\alpha = 2$ deg for $M = 0.60$: a) RANS, and b) DES (instantaneous).

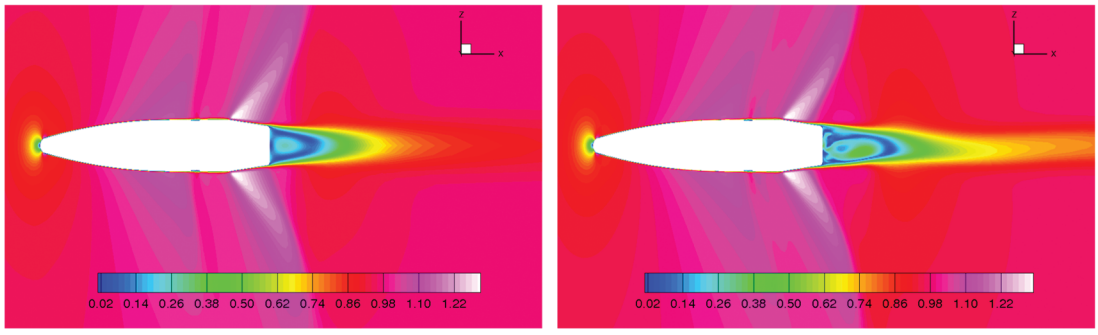

a) b)

Fig. 7 Comparison of Mach number contours on the symmetry plane at $\alpha = 2$ deg for $M = 0.98$: a) RANS, and b) DES (instantaneous).

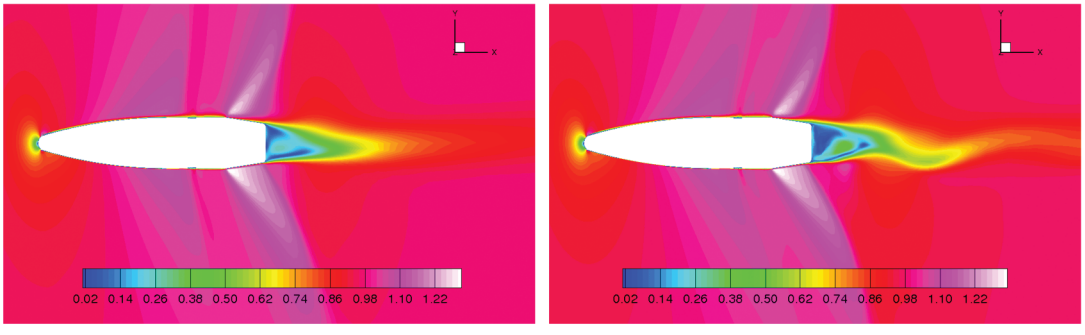

a) b)

Fig. 8 Comparison of Mach number contours on the pitch plane at $\alpha = 5$ deg for $M = 0.98$: a) RANS, and b) DES (instantaneous).

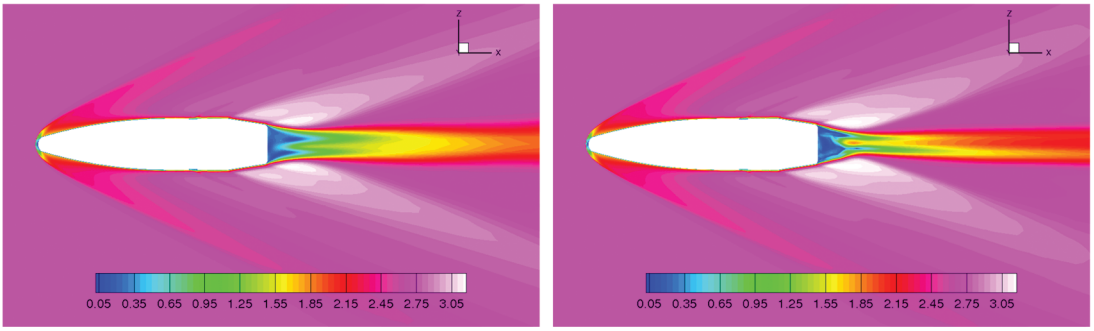

a) b)

Fig. 9 Comparison of Mach number contours on the symmetry plane at $\alpha = 5$ deg for $M = 2.7$: a) RANS, and b) DES (instantaneous).

unsteadiness, but the shift in the shock position was not very significant (Figs. 7 and 8). Note the slight extension of the recirculation region predicted by DES near the base. This is consistent with other DES studies (for example, see [31]).

Figure 9 plots the Mach number contours at the symmetry plane for $M = 2.7$ at a 5 deg angle of yaw. Both RANS and DES predict similar base flow. The flow structure at the base is possibly due to separation of the vortex sheet due to a high angle of yaw [4]. This was observed at all Mach numbers for a 5 deg angle of yaw. At lower angles, this feature of the base flow is not as pronounced. Further, significant movement was observed in the position of the recompression shock for lower supersonic Mach numbers. The pattern in the shift of the recompression shock is governed by the instability in the separated shear layer. No oscillatory flow similar to the subsonic or transonic flowfields is observed, despite the large angle of yaw for high Mach number flows in the unsteady simulations.

The detached eddy simulations capture the right flow physics, such as asymmetric flowfield and oscillatory wake, in addition to resolving an increased range of length scales at the base. Moreover, shock unsteadiness is captured by DES in the transonic regime. RANS, on the other hand, does not exhibit any such characteristics.

C. Data Comparison

In this section we compare our simulation results with the experimental data obtained at the U.S. Army Research Laboratory by McCoy [19]. As in [18], we compare our simulation results to the M33 and M8 experiments. These projectiles have the same external dimensions and differ only in surface details such as rolled vs machined cannelures [19]. McCoy presents data for a wide range of total angles of yaw, α_t, which combines the yaw angle and sideslip angle as $\alpha_t = \sqrt{\alpha^2 + \beta^2}$. Our simulations were performed at yaw angles of 0, 2, and 5 deg; therefore, we make direct comparisons to only a subset of the experimental data. For example, for the $\alpha = 2$ deg simulations, we use the $\alpha_t = 2 \pm 1$ deg data for comparison. This introduces some degree of uncertainty in the comparisons because the experimental conditions do not discriminate between yaw and sideslip and no particular shot is at exactly the conditions simulated. Silton [18] used the Aeroballistic Research Facility data analysis system to reduce the experimental data to provide improved estimates of the $\alpha = 0$ deg drag coefficient and the Magnus moment coefficient derivatives at yaw angles of 2 and 5 deg. Silton [18] reports the estimated experimental error of the aerodynamic forces and moments, and we include the corresponding error bars in our plots.

In this section we also compare our simulations to the RANS results of Silton [18], who used a realizable k–ϵ turbulence model. Our RANS and DES results were obtained with the Spalart–Allmaras turbulence model. Thus, we expect that the differences between the RANS of Silton and our present RANS are primarily due to the turbulence models. Likewise, the differences between our present RANS and DES results can be attributed to how the two turbulence modeling approaches represent the flowfield. In particular, DES should capture more of the unsteady separated flow in the base region. These comparisons should provide the reader with an understanding of how the Reynolds-averaging approximation affects the simulation of the projectile aerodynamics.

Figure 10 compares the 0 yaw drag coefficient. Note the excellent agreement between the DES and experiment for all Mach numbers. By contrast, RANS overpredicts the drag coefficient, particularly around $M = 1$. We see similar behavior of the comparisons at $\alpha = 2$ and 5 deg, as shown in Fig. 11. At low angles of attack, the main difference between DES and RANS is in how the separated base flow is modeled. DES captures the unsteady separated flow physics, whereas RANS produces a steady-state flowfield. Thus, the improved drag prediction is a result of the improved modeling of the base flow and better prediction of the base pressure.

There is a notable difference between the RANS simulations in the low supersonic regime. As seen in Fig. 10, the present RANS predicts a value of C_{D0} that is above that of [18] at $M = 1.1$, and then below the previous results at $M = 1.5$. The reason for this behavior is probably due to the use of different turbulence models, because that is the primary difference between the simulations.

Figure 12 shows the variation of the roll-damping coefficient. The simulations show the same trend, with overprediction at subsonic speeds and underprediction as the Mach number increases from $M = 1$. The marked difference in predicting C_{lp} was discussed in [18]. This has been attributed to the fact that the engraving on the projectile at the time of firing is not modeled. In a recent study [32,33], the engraving was found to have a large effect on the roll-damping coefficient. Also, note that the simulations should not be compared with the experiments in the supersonic regime because the experimental data points were selected so that they provide a good fit to the yawing motion. This results in a nearly constant value for C_{lp} above $M = 1$. Here, the difference between RANS and DES is smaller than the difference between the two RANS simulations. Therefore, the roll-damping coefficient is not particularly sensitive to

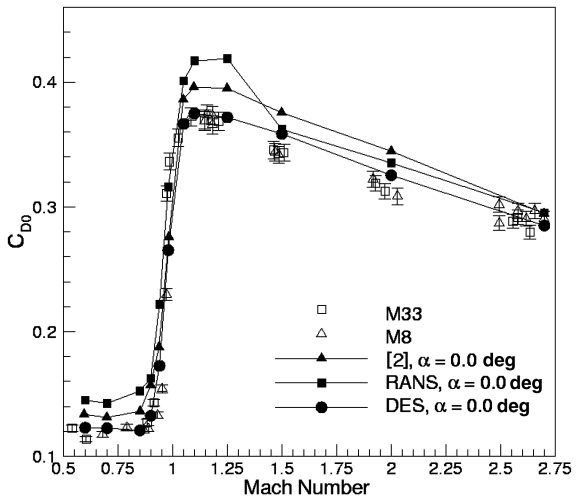

Fig. 10 Zero yaw drag coefficient vs Mach number.

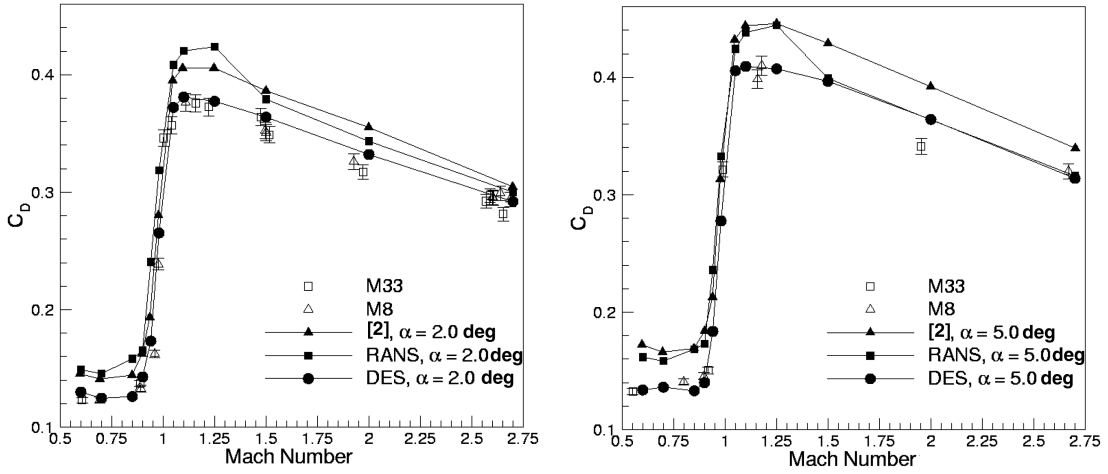

a) b)

Fig. 11 Drag coefficient comparison: a) $\alpha = 2$ deg, and b) $\alpha = 5$ deg.

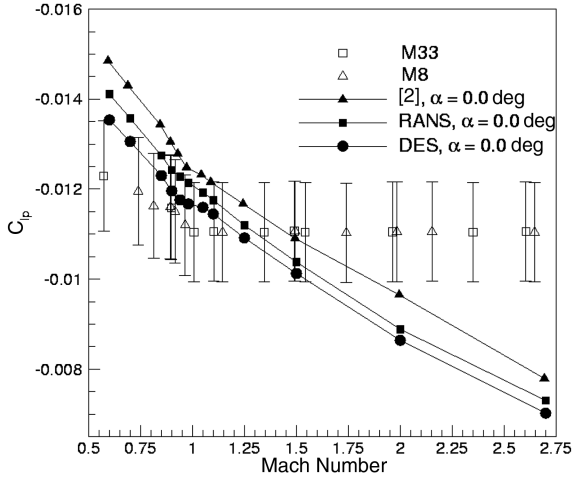

Fig. 12 Roll-damping coefficient vs Mach number.

the additional flow physics captured by DES, but is sensitive to the turbulence closure model.

The overturning moment coefficient, $C_{M\alpha}$, is compared in Fig. 13 for $\alpha = 2$ and 5 deg. Here we have plotted only the data with α_t within 1 deg of the relevant values of α. In general, all simulations predict the correct trends in the data, with a very large value of $C_{M\alpha}$ near $M = 1$. The simulations approximately bracket the error bars in the data, with DES predicting larger values than either of the RANS results. Thus, DES does not provide an obvious benefit for the prediction of the overturning moment, at least within the limitations of the present experimental data.

The plots for the lift-force coefficient derivative, $C_{L\alpha}$, for RANS and DES are shown in Fig. 14. Again, the simulations approximately bracket the experimental data, especially given the larger uncertainty in these measurements. It is interesting to note that at supersonic conditions the present results predict larger values of $C_{L\alpha}$ relative to the RANS results of Silton. Clearly, the turbulence model has a very significant effect on this coefficient at supersonic conditions. DES predicts the lowest value of $C_{L\alpha}$ at subsonic conditions, whereas the RANS results are closer to one another. Thus, DES predicts a more significant variation in the lift-curve slope around the sonic condition than RANS. It is interesting to note that the DES approach gives better predictions of drag and overturning moments than RANS, and yet, for the lift coefficient derivative, its predictions appear to be less accurate.

The variation of the Magnus moment coefficient derivative for the 2 and 5 deg cases is shown in Fig. 15. The relevant experimental data are taken from [18]. First, let us consider the Magnus moment coefficient derivative at $\alpha = 2$ deg, shown in Fig. 15a. The present RANS results and those in [18] predict the same trend and show good agreement with each other, whereas the DES predicts a very different behavior for Mach numbers less than 1.5. The experimental data show a wide variation for these conditions, making it difficult to

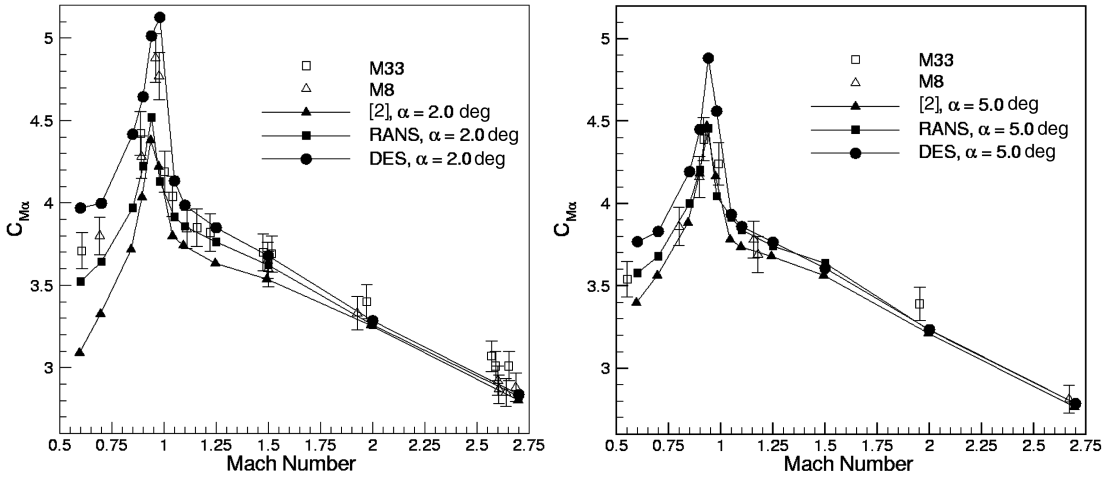

a) b)

Fig. 13 Overturning moment coefficient comparison: a) $\alpha = 2$ deg, and b) $\alpha = 5$ deg.

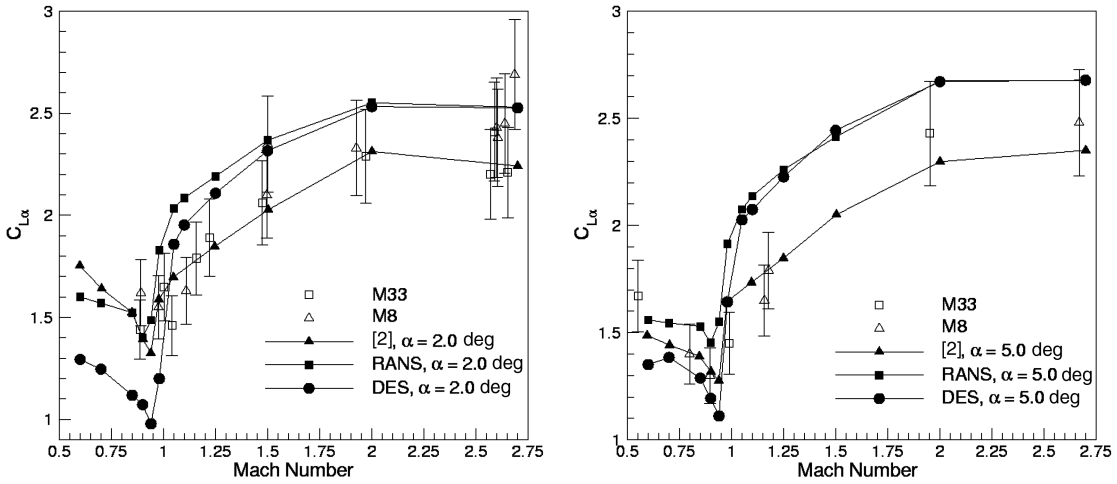

Fig. 14 Lift coefficient derivative comparison: a) $\alpha = 2$ deg, and b) $\alpha = 5$ deg.

determine if the DES approach produces more accurate results. The main difference between the flows produced by the two methods is that the DES is unsteady and results in an unsteady $C_{Mp\alpha}$. In our simulations, we have averaged the DES data over extended periods (more than 500 flow times) to obtain our best estimate of this moment coefficient. This type of variation in $C_{Mp\alpha}$ at a small yaw angle was also observed by DeSpirito and Heavey [17] for a different projectile, although it is important to note that, in the supersonic regime, there is a difference in the sign between the two studies. Because of the inconsistency of the present experimental data, we cannot determine if the DES results are accurate. However, it is clear that the unsteady flow physics modeled by DES have a significant effect on the Magnus moment derivative at low yaw angles for subsonic and low supersonic conditions. The steady-state RANS simulations cannot capture this effect.

In contrast to the 2 deg yaw case, the DES results for the 5 deg yaw case follow the RANS behavior, as can be seen in Fig. 15b. The experimental data are also more self-consistent, and the simulations largely agree with the measurements. The RANS results of [18] at low Mach numbers predict larger values of $C_{Mp\alpha}$ than the present RANS. Again, this should be attributed to differences in the RANS models used in the studies. One other discrepancy is that DES predicts a notably larger value of this coefficient in the transonic regime.

The primary reason that the DES results differ from the steady-state RANS computations is that DES predicts unsteadiness in the projectile base and wake regions. In subsonic flows, the effect of this unsteadiness can be felt upstream, producing an unsteady variation in forces and moments acting on the projectile. According to the present DES results, the Magnus moment is affected more than the other forces and moments. At supersonic speeds, the effect of the unsteady wake is not transmitted upstream, and this causes both the steady-state RANS simulations and the DES to essentially give the same results. In the transonic regime, in addition to the effect of the unsteady wake, the unsteady shock motion also affects the forces and moments. This effect can be seen by considering Fig. 16a, which shows the variation of the Magnus moment coefficient for three representative Mach numbers at $\alpha = 2$ deg. Note that, for the subsonic and transonic cases, C_{Mp} has a strong temporal variation, with no clear mean value. In particular, the coefficient for the transonic case varies over a large time interval and, for this reason, the transonic cases were run for longer periods to obtain meaningful statistics. Even after running the transonic simulations for a long time (about 500 flow times) for the 2 deg yaw case, the coefficients still did not converge as well as for the other Mach numbers. As shown in Fig. 16b, this effect is significantly reduced at a 5 deg yaw angle.

The large time scale observed in the variation of the Magnus moment for the transonic case corresponds to the shock movement and the resulting change in the center of pressure. This phenomenon, which cannot be captured by the steady-state simulations, is represented by DES, and this enables it to better predict the transonic behavior. In comparison to RANS, DES predicts a different force loading with a different center of pressure. This causes larger differences between DES and RANS in predicting the moments than

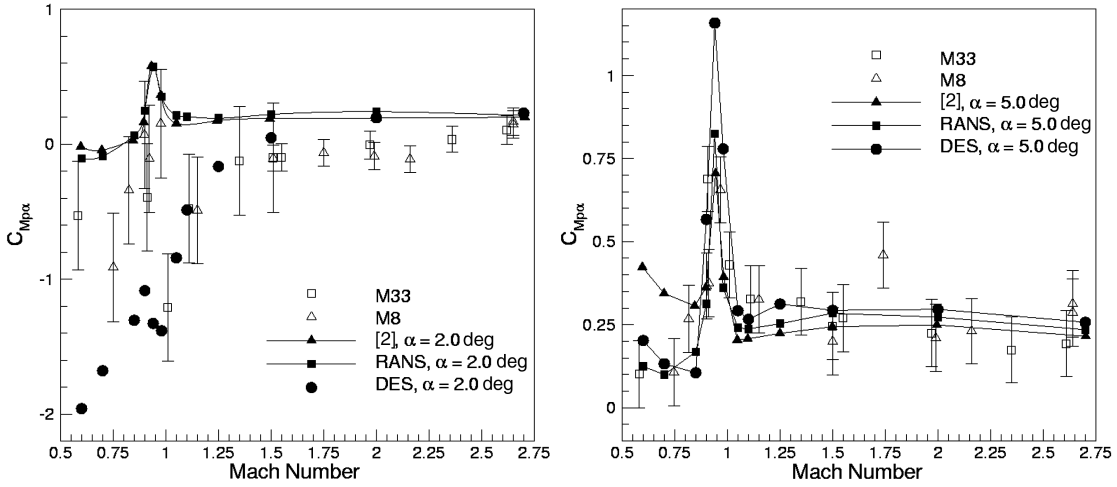

Fig. 15 Magnus moment coefficient derivative comparison: a) $\alpha = 2$ deg, and b) $\alpha = 5$ deg.

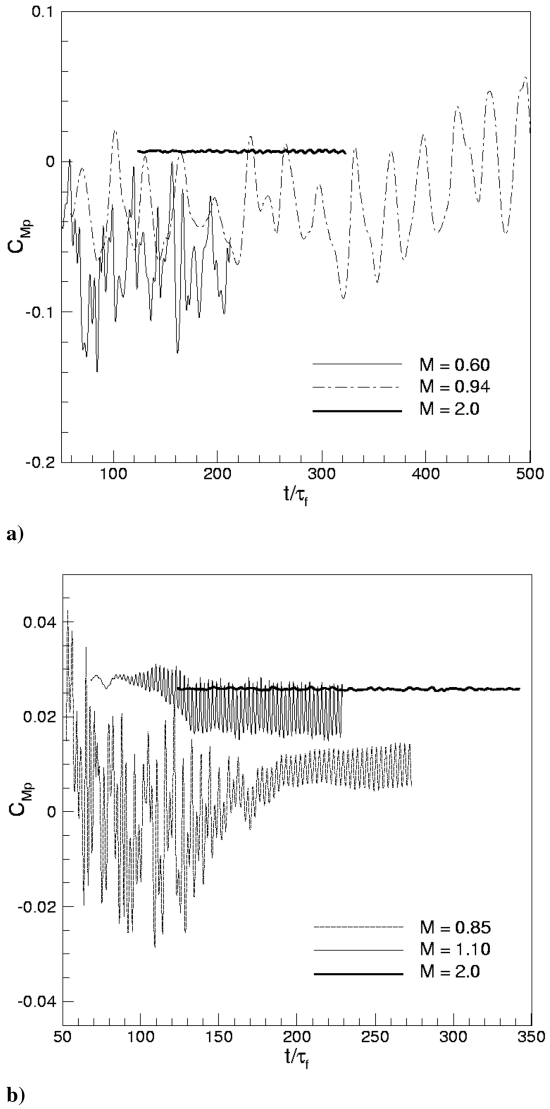

Fig. 16 Magnus moment coefficient vs time for different Mach numbers: a) $\alpha = 2$ deg, and b) $\alpha = 5$ deg.

it does in predicting the forces, as seen in the overturning moment coefficient (Fig. 13b) and the Magnus moment coefficient derivative (Fig. 15). This also helps explain the larger discrepancy in moment predictions between DES and RANS at transonic speeds.

IV. Conclusions

In this paper, we present the results of a comparison between unsteady detached eddy simulations and steady-state RANS results for a spinning projectile. We consider three yaw angles at 12 Mach numbers, with the goal of understanding how DES and RANS simulations differ from one another. In particular, we address how the additional flow physics captured by the DES changes the predicted projectile aerodynamics. We also compare our results to those of Silton [18] to assess how different RANS models affect the results. The drag is well predicted at all Mach numbers, with DES giving more accurate results in the transonic and low supersonic regime. We attribute this difference to the modeling of the unsteady base flow and the improved base pressure obtained with DES. The lift coefficient derivative is less sensitive to the unsteady effects modeled by DES and appears to be more dependent on the underlying turbulence model used in the simulations. However, DES predicts a lower value of $C_{L\alpha}$ at subsonic conditions. Similarly, the overturning moment is less affected by the unsteady effects, except near $M = 1$ where it predicts larger values than either of the RANS simulations. The largest difference between RANS and DES is found in the Magnus moment derivative predictions. For a yaw angle of 2 deg, the two RANS simulations agree with one another, whereas the DES predicts a very different behavior below speeds corresponding to $M = 1.5$. We attribute this effect to the modeling of unsteady wake shedding and shock motion. Given the limitations of the experimental data, it is not possible to determine if DES captures this effect correctly. Interestingly, at $\alpha = 5$ deg, this effect is much less significant. Generally, the differences between the present DES and RANS results are of a similar magnitude to those between the RANS simulations, indicating that the turbulence model plays a major role in these simulations. These comparisons show that DES is a viable tool for simulating spinning projectile aerodynamics, and the additional unsteady flow physics captured by the approach may improve the predictions.

References

[1] Lin, T. C., and Rubin, S. G., "Viscous Flow over Spinning Cones at Angle of Attack," *AIAA Journal*, Vol. 12, No. 7, 1974, pp. 975–985. doi:10.2514/3.49389

[2] Sturek, W. B., Dwyer, H. A., Kayser, L. D., and Nietubicz, C. J., "Computations of Magnus Effects for a Yawed, Spinning Body of Revolution," *AIAA Journal*, Vol. 16, No. 7, 1978, pp. 687–692.

[3] Wang, K. C., "Boundary Layer over Spinning Blunt Body of Revolution at Incidence Including Magnus Forces," *Proceedings of the Royal Society of London, Series A: Mathematical and Physical Sciences* Vol. 363, No. 1714, Nov. 1978, pp. 357–380. doi:10.1098/rspa.1978.0173

[4] Covert, E. E., and Eberhardt, D. S., "Vortex Model for Magnus Forces at Low Speeds, Spins and Angles," *AIAA Journal*, Vol. 20, No. 2, 1982, pp. 235–242. doi:10.2514/3.7906

[5] Seigner, A., and Ringel, M., "Magnus Effects at High Angles of Attack and Critical Reynolds Numbers," *AIAA Journal*, Vol. 23, No. 3, 1986, pp. 237–244.

[6] Sturek, W. B., and Schiff, L. B., "Numerical Simulations of Steady Supersonic Flow over Spinning Bodies of Revolution," *AIAA Journal*, Vol. 20, No. 12, 1982, pp. 1724–1731. doi:10.2514/3.8011

[7] Qin, N., Lublow, D. K., Shaw, S. T., Edwards, J. A., and Dupois, A., "Calculation of Pitch Damping Coefficients for Projectiles," AIAA Paper 0097-0405, Jan. 1997.

[8] Guidos, B. J., and Chung, S. K., "Computational Flight Design of 0.50 Caliber Limited-Range Training Ammunition," AIAA Paper 1995-0063, Jan. 1995.

[9] Nietibucz, C. J., Sturek, W. B., and Heavey, K. R., "Computations of Projectile Magnus Effect at Transonic Velocities," *AIAA Journal*, Vol. 23, No. 7, 1985, pp. 998–1004. doi:10.2514/3.9030

[10] Sahu, J., and Heavey, K. R., "Application of CFD to High Angle of Attack Missile Flowfields," AIAA Paper 2000-4210, Aug. 2000.

[11] DeSpirito, J., Harris, L. E., Weinacht, P., and Sahu, J., "Computational Fluid Dynamics Analysis of a Missile with Grid Fins," *Journal of Spacecraft and Rockets*, Vol. 38, No. 5, 2001, pp. 711–718.

[12] Park, S. H., and Kwon, J. H., "Navier-Stokes Computations of Stability Derivatives for Symmetric Projectiles," AIAA Paper 2004-14, Jan. 2004.

[13] Sahu, J., and Heavey, K. R., "Time-Accurate Numerical Prediction of Free Flight Aerodynamics of a Finned Projectile," AIAA Paper 2005-5817, Aug. 2005.

[14] Spalart, P. R., and Allmaras, S. R., "A One-Equation Turbulence Model For Aerodynamic Flows," AIAA Paper 1992-0439, Jan. 1992.

[15] Strelets, M., "Detached Eddy Simulation of Massively Separated Flows," AIAA Paper 2001-0879, Jan. 2001.

[16] Squires, K. D., Forsyth, J. R., Morton, S. A., Strang, W. Z., Wurtzler, K. E., Tomaro, R. F., Grismer, M. J., and Spalart, P. R., "Progress on Detached-Eddy Simulation of Massively Separated Flows," AIAA Paper 2002-1021, Jan. 2002.

[17] DeSpirito, J., and Heavey, K. R., "CFD Computation of Magnus Moment and Roll Damping Moment of a Spinning Projectile," AIAA Paper 2004-4713, Aug. 2004.

[18] Silton, S., "Navier-Stokes Computations for a Spinning Projectile from Subsonic to Supersonic Speeds," *Journal of Spacecraft and Rockets*, Vol. 42, No. 2, 2005, pp. 223–231

[19] McCoy, R. L., "The Aerodynamic Characteristics of .50 Ball, M33, API, M8, and APIT, M20 Ammunition," U.S. Army Ballistic Research

Lab. BRL-MR-3810, Aberdeen Proving Ground, MD, Jan. 1990.
[20] Nompelis, I., Drayna, T., and Candler, G., "Development of Hybrid Unstructured Implicit Solver for the Simulation of Reacting Flows over Complex Geometries," AIAA Paper 2004-2227, July 2004.
[21] GridPro/az3000, Ver. 4.3, Program Development Co., White Plains, NY.
[22] Spalart, P. R., "Young Person's Guide to Detached-Eddy Simulation Grids," NASA Technical Rept. CR 2001-211032, July 2001.
[23] Druguet, M.-C., Candler, G., and Nompelis, I., "Effects of Numerics on Navier-Stokes Computations of Hypersonic Double-Cone Flows," *AIAA Journal*, Vol. 43, No. 3, 2005, pp. 616–623. doi:10.2514/1.6190
[24] Kim, S.-E., Makarov, B., and Caraeni, D., "A Multi-Dimensional Linear Reconstruction Scheme for Arbitrary Unstructured Grids," AIAA Paper 2003-3990, June 2003.
[25] Catris, S., and Aupoix, B., "Density Correction for Turbulence Models," *Aerospace Science and Technology*, Vol. 4, No. 1, Jan. 2000, pp. 1–11. doi:10.1016/S1270-9638(00)00112-7
[26] Wright, M. J., Candler, G. V., and Bose, D., "Data-Parallel Line Relaxation Method for the Navier Stokes Equations Using Gauss-Seidel Line Relaxation," *AIAA Journal*, Vol. 36, No. 9, 1998, pp. 1603–1609.
[27] Wright, M. J., Candler, G. V., and Prampolini, M., "Data-Parallel Lower Upper Relaxation Method for the Navier-Stokes Equations," *AIAA Journal*, Vol. 34, No. 7, 1996, pp. 1371–1377. doi:10.2514/3.13242
[28] Nompelis, I., Drayna, T., and Candler, G., "A Parallel Unstructured Implicit Solver for Hypersonic Reacting Flow Simulation," AIAA Paper 2005-4867, June 2005.
[29] Subbareddy, P., and Candler, G. V., "Detached Eddy Simulation of Supersonic Base Flow with Bleed," AIAA Paper 2004-66, Jan. 2004.
[30] Squires, K. D., "Detached-Eddy Simulation: Current Status and Perspectives," *Proceedings of Direct and Large-Eddy Simulation-5*, Kluwer, Dordrecht, The Netherlands, August 2003, pp. 465–480.
[31] Subbareddy, P., and Candler, G. V., "Numerical Investigations of Supersonic Base Flows Using DES," AIAA Paper 2005-886, Jan. 2005.
[32] Weinacht, P., "Validation and Prediction of the Effect of Rifling Grooves on Small-Caliber Ammunition Performance," AIAA Paper 2006-6010, 2006.
[33] Silton, S. I., and Webb, D. W., "Experimental Determination of the Effect of Rifling Grooves on the Aerodynamics of Small Caliber Projectiles," AIAA Paper 2006-6009, 2006.

M. Costello
Associate Editor